POLITECNICO DI TORINO
Repository ISTITUZIONALE

Improved modeling technique of metamaterials

Original
Improved modeling technique of metamaterials / Augello, R., Carrera, E.. - In: MECHANICS OF ADVANCED MATERIALS AND STRUCTURES. - ISSN 1537-6494. - 33:1(2026). [10.1080/15376494.2026.2659955]

Availability:
This version is available at: 11583/3017454 since: 2026-11-03T10:39:09Z

Publisher:
Taylor and Francis

Published
DOI:10.1080/15376494.2026.2659955

Terms of use:

This article is made available under terms and conditions as specified in the corresponding bibliographic description in the repository

Publisher copyright

(Article begins on next page)

21 November 2026



Mechanics of Advanced Materials and Structures

ISSN: 1537-6494 (Print) 1537-6532 (Online) Journal homepage: www.tandfonline.com/journals/umcm20

Improved modeling technique of metamaterials

Riccardo Augello & Erasmo Carrera

To cite this article: Riccardo Augello & Erasmo Carrera (2026) Improved modeling technique of metamaterials, Mechanics of Advanced Materials and Structures, 33:1, 2659955, DOI: 10.1080/15376494.2026.2659955

To link to this article: https://doi.org/10.1080/15376494.2026.2659955

© 2026 The Author(s). Published with license by Taylor & Francis Group, LLC

Published online: 04 May 2026.

Submit your article to this journal

Article views: 545

View related articles

View Crossmark data

Citing articles: 3 View citing articles

Full Terms & Conditions of access and use can be found at https://www.tandfonline.com/action/journalInformation?journalCode=umcm20

MECHANICS OF ADVANCED MATERIALS AND STRUCTURES
2026, VOL. 33, NO. 1, 2659955
https://doi.org/10.1080/15376494.2026.2659955

Taylor & Francis
by informa

ORIGINAL ARTICLE

OPEN ACCESS Check for updates

Improved modeling technique of metamaterials

Riccardo Augello and Erasmo Carrera

Mul Group Department of Mechanical and Aerospace Engineering, Politecnico di Torino, Torino, Italy

ABSTRACT

Geometry-driven metamaterials such as auxetic and chiral offer negative Poisson's ratios, vanishing shear stiffness, and programmable multi-stability, but their slender struts and large rotations overwhelm conventional finite-element meshes. A streamlined framework that couples classical finite elements with the Carrera Unified Formulation (CUF) resolves cross-sectional deformation through higher-order beam expansions, reproducing three-dimensional behavior while retaining a one-dimensional model. Contrary to the conventional beam definition, in this study the structural beam axis is aligned with the thickness of the sandwich panel, while the cross-section extends across its width. This particular application is useful to highlight the flexibility of CUF in modeling any structural configuration as an advanced 1D element. Representative static linear analyses are presented of popular metamaterial designs.

ARTICLE HISTORY
Received 10 March 2026
Accepted 19 March 2026

KEYWORDS
Metamaterial; finite element method; static analysis; reentrant; chiral

1. Introduction

In the past decade, lattice-based metamaterials have emerged as a central paradigm in architected materials, where macroscopic behavior is governed predominantly by geometry rather than by base-material chemistry. Built from periodically replicated unit cells (UCs), these lattices are carefully designed so that their architecture enforces unconventional global responses. By judiciously tailoring the unit-cell topology and slenderness, properties can be targeted with high precision: from auxetic systems exhibiting a negative Poisson's ratio [1–4], to pentamodes that nearly suppress shear deformation [5], to strongly nonlinear responses driven by large bending and elastic instabilities. Such instabilities have been exploited to realize programmable shape morphing under compression or tension in both mono-stable [6, 7] and multi-stable [8–11] regimes, as well as under thermal loading [12]. Architected lattices thus provide a versatile platform for mechanical functionality that is difficult, if not impossible, to achieve with homogeneous solids.

Because the global response of a lattice is rooted in its microscopic layout, a substantial body of work has focused on establishing analytical links between UC geometry and effective properties. Early contributions based on Bernoulli–Euler and Timoshenko beam theories derived closed-form expressions for the elastic moduli and Poisson's ratio of cuboid microlattices [13]. Building on that framework, Ahmadi et al. formulated relationships for stiffness, buckling load, and yield stress in diamond-shaped UCs manufactured by selective laser melting; they reported excellent agreement with experiments at low relative densities, although Euler–Bernoulli predictions progressively departed from measurements at higher densities [14]. Similar unit-cell level models have successfully reproduced small-strain responses of 3D-printed PLA biomaterials [15]. These studies collectively demonstrate that simplified beam-based descriptions can be highly predictive in well-controlled regimes, but they also expose limitations when geometries become more intricate or loading drives the structure into large deformation regimes.

Within the broader class of negative-Poisson-ratio (NPR) materials, reentrant honeycombs are among the most widely studied due to their geometric simplicity and tunability [16]. Numerous two-dimensional variants, such as curved-edge [17, 18] and hierarchical configurations [19, 20], have been proposed and demonstrated. However, their intrinsically planar nature constrains the design space and restricts the range of achievable mechanical responses. Extending reentrant concepts to three dimensions unlocks richer auxetic behavior and enhanced energy absorption. Three-dimensional NPR lattices have been realized both *via* additive manufacturing [21–23] and through mechanical assembly strategies. Li's 3D reentrant lattice, experimentally validated under compression [24], and its augmented versions with additional struts, capable of broad-range stiffness and Poisson's-ratio tuning [25], are notable examples. Interlocking-assembly approaches further reduce fabrication overhead compared to purely layer-wise printing [26], making large-scale auxetic structures increasingly practical.

CONTACT Riccardo Augello riccardo.augello@polito.it Mul2 Group Department of Mechanical and Aerospace Engineering, Politecnico di Torino, Corso Duca degli Abruzzi 24, 10129 Torino, Italy.

© 2026 The Author(s). Published with license by Taylor & Francis Group, LLC
This is an Open Access article distributed under the terms of the Creative Commons Attribution License (http://creativecommons.org/licenses/by/4.0/), which permits unrestricted use, distribution, and reproduction in any medium, provided the original work is properly cited. The terms on which this article has been published allow the posting of the Accepted Manuscript in a repository by the author(s) or with their consent.

Chiral lattices, first envisaged in the pioneering works of Wojciechowski [27, 28], offer another prominent route to unusual mechanical behavior. These architectures combine auxeticity with remarkable wave-manipulation capabilities, including vibration attenuation and band-gap formation [29, 30]. Subsequent studies have shown that their dispersion characteristics and band-gap locations are exquisitely sensitive to geometric details [31]. Recent three-dimensional realizations have demonstrated fine control over elastic-wave polarization and trajectory [32], while detailed dispersion analyses confirm direction-selective propagation in auxetic chiral lattices [33]. Such properties are particularly attractive for vibration isolation, acoustic cloaking, and noise reduction, where geometry-driven spectral tailoring is a key design objective [31, 34, 35].

Accurately simulating the rich mechanics of reentrant, chiral, and related lattices requires numerical tools capable of capturing rigid-body-like motions, large rotations, localized bending, and steep stress gradients, without incurring prohibitive computational costs. Conventional finite element methods (FEM), though extremely versatile, often struggle in this context: faithfully resolving the slender members and fine architectural details typically demands very dense 3D meshes, leading to large models and long runtimes. Several targeted alternatives have been proposed, including isogeometric analysis [36–38], homogenisation-based strategies [39–41], and reduced-order or component-based models [42, 43]. These approaches have alleviated computational burdens in specific settings, yet they often focus on narrow classes of geometries or loading conditions, and a broadly applicable, high-fidelity framework remains elusive.

A general and unified solution is offered by integrating classical FEM with the Carrera Unified Formulation (CUF) [44, 45]. CUF enriches one-dimensional finite elements through tailored cross-sectional expansion functions that recover complex deformation modes, including warping and local bending, within a beam-like description. When Lagrange expansions are adopted, the method accommodates arbitrarily intricate cross-sections and multi-material layouts, making it particularly suited to the convoluted geometries of mechanical metamaterials. In this setting, slender beams with detailed cross-sectional kinematics can be assembled into large, three-dimensional lattice architectures while keeping the global number of degrees of freedom within manageable limits. The resulting CUF-based framework is capable of reproducing the essential physics of complex lattices, static response, buckling, and dynamic behavior, with high accuracy and markedly reduced computational overhead [46, 47]. This opens the door to systematic, cost-effective design, optimization, and parametric exploration of next-generation metamaterials featuring chiral, reentrant, and hybrid architectures.

2. One-dimensional beam finite element for the modeling of metamaterial structure

The Carrera Unified Formulation (CUF) revisits classical structural modeling to make it compatible with the geometric complexity typical of lattice and sandwich metamaterials. Instead of relying on full three-dimensional (3D) or two-dimensional (2D) finite element models to achieve high fidelity, CUF enables such structures to be represented as one-dimensional (1D) elements while still resolving rich deformation patterns. Traditional 3D/2D finite element formulations are accurate but computationally demanding, especially when modeling fine architectural details. Conversely, standard 1D beam theories are efficient, but they cannot capture cross-sectional warping, thickness-wise gradients, or strong anisotropies, which are crucial in architected and layered materials. CUF overcomes these limitations by employing high-order Lagrange polynomials to discretize the cross-section, thereby enriching the representation of both geometry and mechanical response.

In conventional 1D beam modeling, the beam axis is aligned with the longest structural dimension. In the framework of classical beam theory, a beam is a prismatic elastic body whose length is much larger than its transverse dimensions, so that the structure can be idealized as a 1D member. The beam axis coincides with the main longitudinal direction, while the two smaller dimensions define the cross-section, as schematically shown in Figure 1. This description is adequate for slender prismatic members with simple geometry, but it becomes restrictive when dealing with nonstandard layouts, curved paths, or architected cross-sections.

CUF introduces a different viewpoint. The beam axis is no longer constrained to follow the predominant structural dimension, and the cross-sectional details are embedded directly in the mathematical model. For the canonical beam, this means that the axis can be reoriented so as to run along a transverse direction, as illustrated in Figure 2. The choice

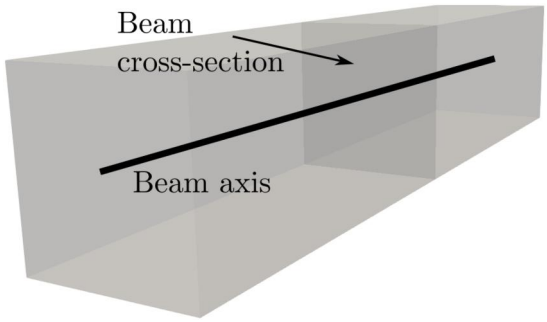


Figure 1. Canonical beam representation.

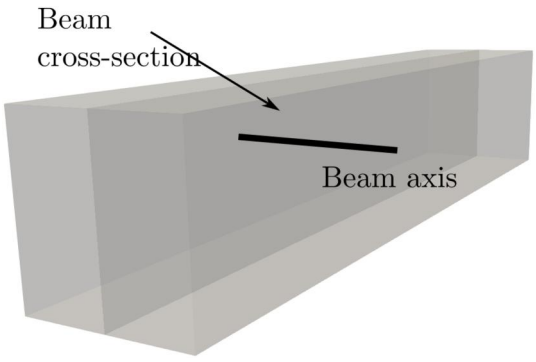


Figure 2. Improved CUF-based beam representation.

of axis becomes a modeling parameter rather than a geometric constraint, and the associated cross-section can be defined according to the needs of the specific application (classical, layered, or lattice-like beam sections).

In practical terms, the CUF-based approach offers two key degrees of freedom for tailoring the model to complex structures:

- Axis alignment. The beam axis can be aligned with any relevant structural dimension, enabling hierarchical descriptions in which different portions of a component (e.g., skins, cores, stiffeners, lattice infills) are modeled with consistent 1D kinematics but along different directions.
- Cross-sectional refinement. The order of the cross-sectional polynomials can be increased to resolve progressively finer geometrical and mechanical features. This allows the user to tune the tradeoff between accuracy and computational cost, from low-order descriptions up to high-fidelity models capable of capturing the behavior of complex sandwich and lattice metamaterials, as considered in this work. Within CUF, the displacement field $\mathbf{u}(x, y, z)$ of a 1D beam element is expressed as

$$\mathbf{u}(x, y, z) = F_\tau(x, z) N_i(y) \mathbf{u}_{\tau i} \quad \tau = 1, 2, ..., M \quad i = 1, 2, ..., N_n \tag{1}$$

where $F_\tau(x, z)$ are the expansion functions defined over the cross-sectional plane, $N_i(y)$ are the interpolation functions along the beam axis, and $\mathbf{u}_{\tau i}$ are the nodal generalized displacements. This tensor-product structure decouples the description of the axial and cross-sectional behavior, providing a unified and flexible framework to model both standard beams and architected metamaterial components.

3. Metamaterial structure with varying cross-section geometry

A reentrant metamaterial is adopted as a benchmark to demonstrate the CUF-based modeling of metamaterial components. The geometry of the structure is reported in Figure 3.

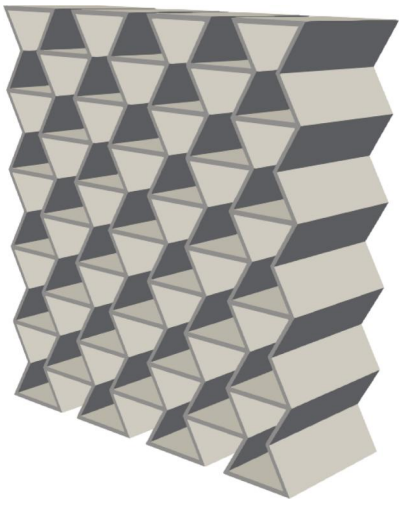


Figure 3. Re-entrant metamaterial structure.

In this framework, exploiting CUF capabilities, the entire structure is described by 1D beam elements whose axis is aligned with the width direction, departing from the conventional beam idealization tied to the longest structural dimension. This is shown in Figure 4.

The cross-sections of the metamaterial is discretized using high-order Lagrange polynomials; this discretization ensures detailed representation of geometry and its mechanical behavior. To maintain displacement continuity between the components, shared Lagrange points are defined at their interfaces, as shown in the discretization of Figure 5. The precise alignment of shared Lagrange points eliminates spurious discontinuities, enabling an accurate description of the coupling between the components.

The use of high-order Lagrange polynomials provides enhanced cross-sectional resolution and an accurate reconstruction of the displacement field, while keeping the number of DOFs significantly lower than that required by high-fidelity 3D finite element models. This aspect is extensively discussed in the following sections. For comparison purposes, the same structure is also analyzed with the commercial FEM code Abaqus.

4. Governing equations

The strain and stress vectors are expressed in the following:

$$\mathbf{u}(x, y, z) = \{u_x, u_y, u_z\}^T \tag{2}$$

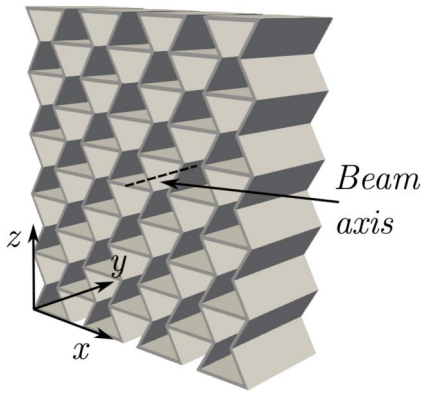


Figure 4. CUF model of the re-entrant metamaterial structure.

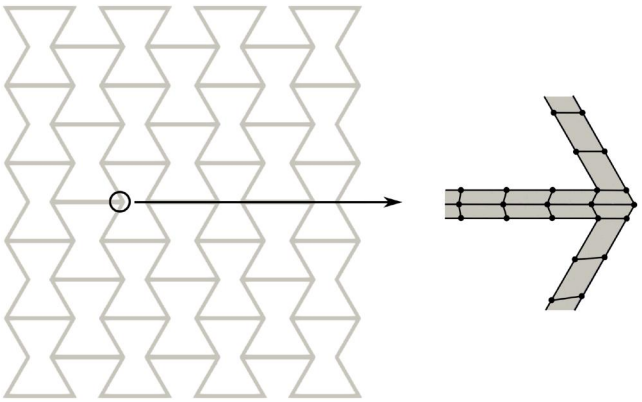


Figure 5. Lagrange elements for the discretization of the re-entrant metamaterial structure.

$$\boldsymbol{\epsilon} = \{\epsilon_{xx}, \epsilon_{yy}, \epsilon_{zz}, \epsilon_{xz}, \epsilon_{yz}, \epsilon_{xy}\}^T;$$
$$\boldsymbol{\sigma} = \{\sigma_{xx}, \sigma_{yy}, \sigma_{zz}, \sigma_{xz}, \sigma_{yz}, \sigma_{xy}\}^T \tag{3}$$

According to linear strain-displacement relations, the strain vector can be written as:

$$\boldsymbol{\epsilon} = \mathbf{D}\mathbf{u} \tag{4}$$

where $\mathbf{D}$ is the differential matrix operator, which explicit form is

$$\mathbf{D} = \begin{bmatrix} \frac{\partial}{\partial x} & 0 & 0 \\ 0 & \frac{\partial}{\partial y} & 0 \\ 0 & 0 & \frac{\partial}{\partial z} \\ \frac{\partial}{\partial z} & 0 & \frac{\partial}{\partial x} \\ 0 & \frac{\partial}{\partial z} & \frac{\partial}{\partial y} \\ \frac{\partial}{\partial y} & \frac{\partial}{\partial x} & 0 \end{bmatrix} \tag{5}$$

The constitutive relation in its linear form is used to relate the stress and the strain as:

$$\boldsymbol{\sigma} = \mathbf{C}\boldsymbol{\epsilon} \tag{6}$$

where $\mathbf{C}$ is material elastic matrix [48, 49]. The governing equations are deduced from the principle of virtual displacements (PVD). For elastic bodies in a state of static equilibrium, the following relationship holds:

$$\delta L_{\text{int}} = \delta L_{\text{ext}} \tag{7}$$

where with δL_{int} is expressed the strain energy variation due to deformations and δL_{ext} stands the work done by external forces on virtual displacements. The variation in internal energy δL_{int} can be expressed as:

$$\delta L_{\text{int}} = \int_V \delta\varepsilon^T \boldsymbol{\sigma}\ dV \tag{8}$$

By employing the displacement functions, geometric relations, and constitutive equations, Equation (8) is rewritten as:

$$\begin{aligned} \delta L_{int} &= \delta \boldsymbol{u}_{js}^T \int_V N_j \mathbf{I} F_s \boldsymbol{D}^T \boldsymbol{C} \boldsymbol{D} F_\tau \mathbf{I} N_i dV \boldsymbol{u}_{i\tau} \\ &= \delta \mathbf{q}_{js}^T \mathbf{k}^{ij\tau s} \mathbf{q}_{i\tau} \end{aligned} \tag{9}$$

Where $\mathbf{k}^{ij\tau s}$ is a 3×3 matrix, called the Fundamental Nucleus (FN) of the mechanical stiffness matrix. The nucleus serves as the basic element from which the stiffness matrix of the entire structure is computed. The fundamental nucleus is expanded across indices i and j to obtain the stiffness matrix.

The virtual work δL_{ext} carried out by the external load p is given by:

$$\delta L_{\text{ext}} = \int_V \delta \boldsymbol{u}^T \mathbf{p}\ dV \tag{10}$$

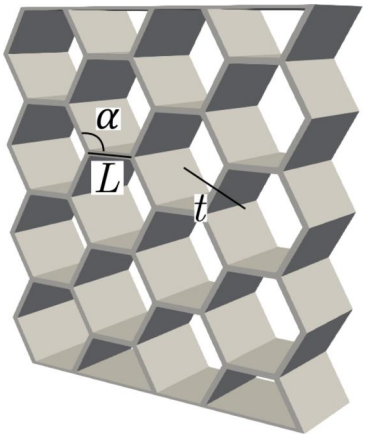


Figure 7. Geometry of the hexagonal metamaterial.

Table 1. DOFs And lateral displacement of the considered analysis. In blue the converged models.

Model	DOFs	Lateral displacement
Abaqus 2D (Figure 7 left)	16,902	0.6234
	98,154	0.6765
	291,930	0.6769
Abaqus 2D (Figure 7 center)	34,830	0.6521
	95,724	0.6736
	677,538	0.6731
CUF 1D (Figure 7 rigth)	19,674	0.6727
	29,511	0.6725
	118,434	0.6724

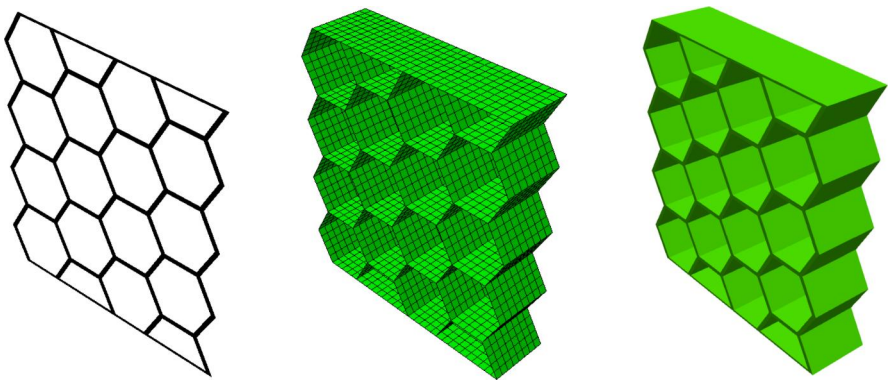


Figure 6. Numerical models of the hexagonal metamaterial. 2D Abaqus models (left and center), CUF 1D model (rigth).

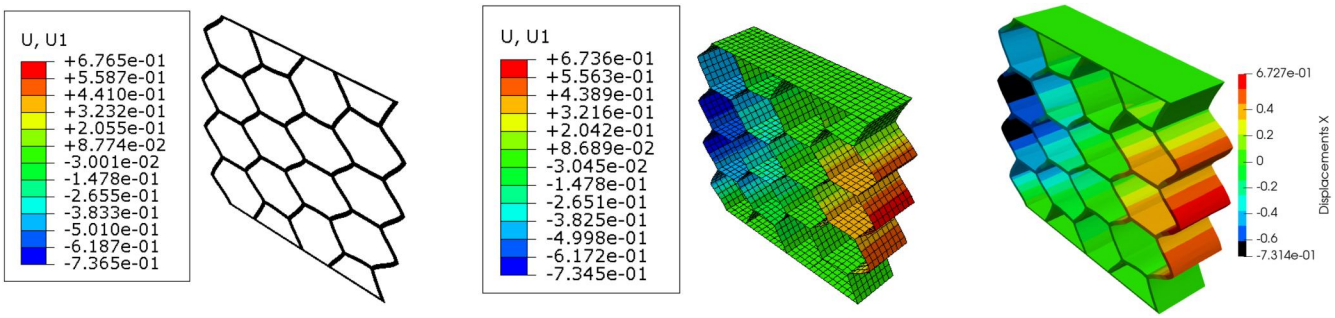


Figure 8. Numerical results of the hexagonal metamaterial. 2D Abaqus models (top), CUF 1D model (bottom).

This equation can be further expanded in the CUF form as:

$$\begin{aligned}\delta L_{\text{ext}} &= \delta \mathbf{q}_{js}^T \int_V N_j \mathbf{I} F_s^j \mathbf{p} \; dV \\ &= \delta \mathbf{q}_{js}^T \mathbf{p}_{js}\end{aligned} \tag{11}$$

where $\mathbf{p}_{js}$ is the 3×1 FN of the load vector. By the combination of Eq. (9) and (11) it is possible to write:

$$\delta \mathbf{q}_{js}^T \mathbf{k}^{ij\tau s} \mathbf{q}_{i\tau} = \delta \mathbf{q}_{js}^T \mathbf{p}_{js} \tag{12}$$

The global stiffness matrix is obtained by the summation over the indices i,j, τ,s following the CUF assembling procedure which interested readers can find in [50].

5. Numerical results

5.1. Hexagonal

The numerical study focuses on a metamaterial with hexagonal topology (Figure 6). The geometry is taken from [51] and it is shown in Figure 7, and $L = 13.4$ mm, $t = 1.3$ mm and $\alpha = 120°$.

Three modeling strategies are considered: (i) a 2D Abaqus model discretized on the surface (in-plane section), (ii) a 2D Abaqus model discretized across the width (transverse section), and (iii) a 3D model based on the Carrera Unified Formulation (CUF), which explicitly represents the metamaterial's three-dimensional geometry. The structure is subjected to a uniform transverse pressure and is clamped along one boundary, with all remaining edges free.

For each model, a mesh-refinement study was performed. Table 1 reports the total number of degrees of freedom (DOFs) together with the lateral displacement values evaluated at a selected control point. The entries that achieved mesh convergence are highlighted in blue in the table.

Compared with the 2D Abaqus reference discretizations, the CUF model reaches the converged response with roughly 20% of the DOFs, indicating a substantial reduction in problem size for a comparable accuracy. This reduction in DOF count translates into lower memory requirements and shorter solution times, while preserving the fidelity needed to capture the characteristic deformation mechanisms of the hexagonal architecture. Finally, Figure 8 illustrates the deformed configurations (plotted with an exaggerated scale for clarity). The three modeling approaches yield consistent global deformation patterns and confirm the expected stiffness trends under transverse loading, further validating the efficiency and accuracy of the CUF-based 3D representation for this class of metamaterials.

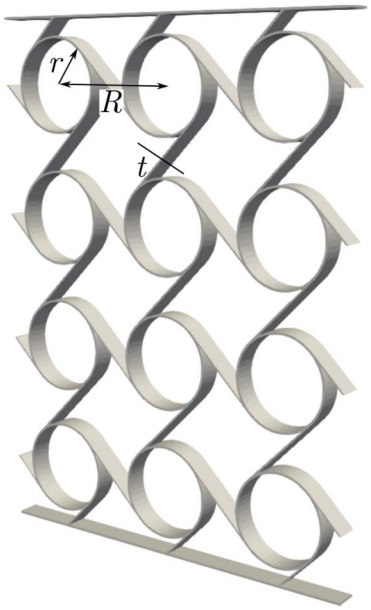


Figure 9. Geometry of the chiral metamaterial.

5.2. Chiral

The second set of numerical results concerns the chiral metamaterial proposed in [52]. The geometry of the analyzed structure is reported in Figure 9, where $t = 1.4$ mm, $R = 117$ mm and $r = 40$ mm. The specimen is composed of 4×3 identical circular hollow unit cells arranged in a periodic pattern.

Four different numerical models are constructed, as illustrated in Figure 10: (i) a 2D Abaqus model discretized on the surface (in–plane section), (ii) a 2D Abaqus model discretized across the width (transverse section), (iii) a fully 3D Abaqus model, and (iv) a 3D CUF-based model, which explicitly represents the metamaterial three-dimensional geometry.

As in the previous benchmark, the structure is clamped at the bottom edge and subjected to a compressive pressure applied at the top edge. The maximum lateral displacement and the corresponding numbers of DOFs for all models are summarized in Table 2; the converged solutions are highlighted in light blue.

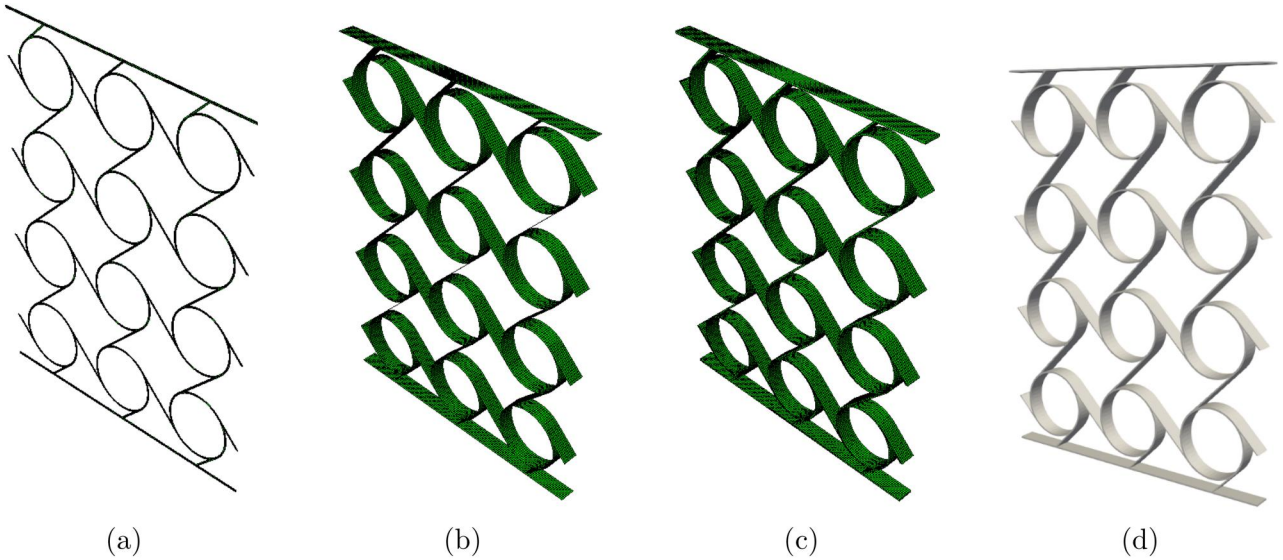


Figure 10. Numerical models of the chiral metamaterial. 2D Abaqus models (a, b), 3D Abaqus model (c) and CUF 1D model (d).

Several considerations can be drawn from these results. The Abaqus 2D model shown in Figure 10b does not provide a reliable prediction of the deformation, even when strongly refined, with more than 2×10^6 DOFs. In contrast, the other three models yield essentially the same lateral displacement, indicating that they all capture the global response of the chiral lattice with good accuracy. Among them, the CUF model is clearly the most efficient: it achieves convergence with a reduction of about 50% of DOFs with respect to the Abaqus 2D in–plane model of Figure 10a, and about 80% with respect to the 3D Abaqus model of Figure 10c. The corresponding deformed configurations are depicted in Figure 11, further confirming that the CUF formulation reproduces the 3D deformation pattern of the chiral metamaterial at a substantially reduced computational cost, making it particularly attractive for parametric studies and design-oriented analyses.

Table 2. DOFs and lateral displacement of the chiral metamaterial. In blue the converged models.

Model	DOFs	Lateral displacement
Abaqus 2D (Figure 10a)	29,166	0.2241
	67,206	0.3098
	180,726	0.1759
	210,076	0.1769
Abaqus 2D (Figure 10b)	125,874	0.1256
	364,770	0.1254
	2,188,146	0.1254
Abaqus 3D (Figure 10c)	132,354	0.2440
	458,604	0.1777
	1,169,910	0.1777
	4,775,640	0.1776
CUF 1D (Figure 10d)	89,682	0.1759
	134,523	0.1760
	568,791	0.1760

5.2.1. Second chiral metamaterial

A modified version of the previous chiral metamaterial is now considered. The geometry and the associated numerical models are shown in Figure 12; unlike the configuration of Figure 9, the circular regions are fully filled with material rather than hollow. As in the previous benchmark, four numerical models are constructed (Figure 12): (i) a 2D Abaqus model discretized on the surface (in–plane section), (ii) a mixed 3D/2D Abaqus model discretized across the width (transverse section), in which the circular regions are modeled with 3D solid elements while 2D elements are used for the ligaments connecting the circles, (iii) a fully 3D Abaqus model, and (iv) a 3D CUF-based model that explicitly represents the three-dimensional geometry of the metamaterial.

The boundary conditions are the same as in the hollow-cell case: the structure is clamped at the bottom edge and subjected to a compressive pressure applied at the top edge. The number of DOFs and the corresponding maximum lateral displacements are reported in Table 3, while the deformed configurations of the converged models are illustrated in Figure 13.

Similar conclusions to those drawn for the hollow-cell lattice can be reached here, but with an important quantitative difference. The converged numerical models now require a larger number of DOFs: the increase in converged DOFs with respect to the previous configuration is about 60% for the Abaqus 2D in–plane model (Figure 12a), 384% for the mixed 2D + 3D Abaqus model (Figure 12b), noting that this compares a purely 2D model with a mixed-dimensional one, 275% for the fully 3D Abaqus model (Figure 12c), and only 24% for the CUF 1D model (Figure 12d). This behavior highlights the adaptability of the CUF formulation, which can accommodate more complex, fully filled geometries with only a modest increase in problem size, while standard FE models experience a much steeper growth in DOFs.

As in the hollow-cell case, the Abaqus model discretized along the width (Figure 12b), here further complicated by the use of 3D elements in the circular regions, fails to deliver accurate and robust predictions of the deformation, despite its very high number of DOFs. In contrast, the remaining three models provide mutually consistent results for the global response. Among them, the CUF model again proves to be the most efficient, achieving convergence with

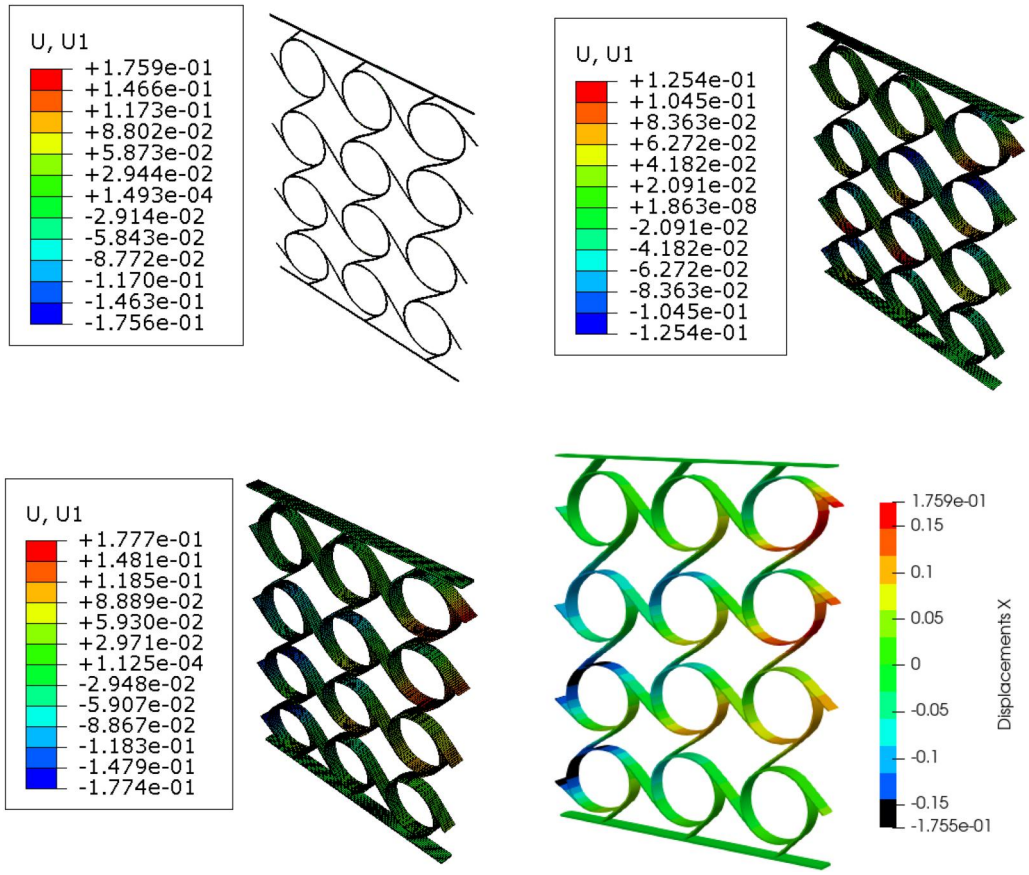


Figure 11. Numerical results of the chiral metamaterial. 2D Abaqus models (top), 3D Abaqus model (bottom left) and CUF 1D model (bottom right).

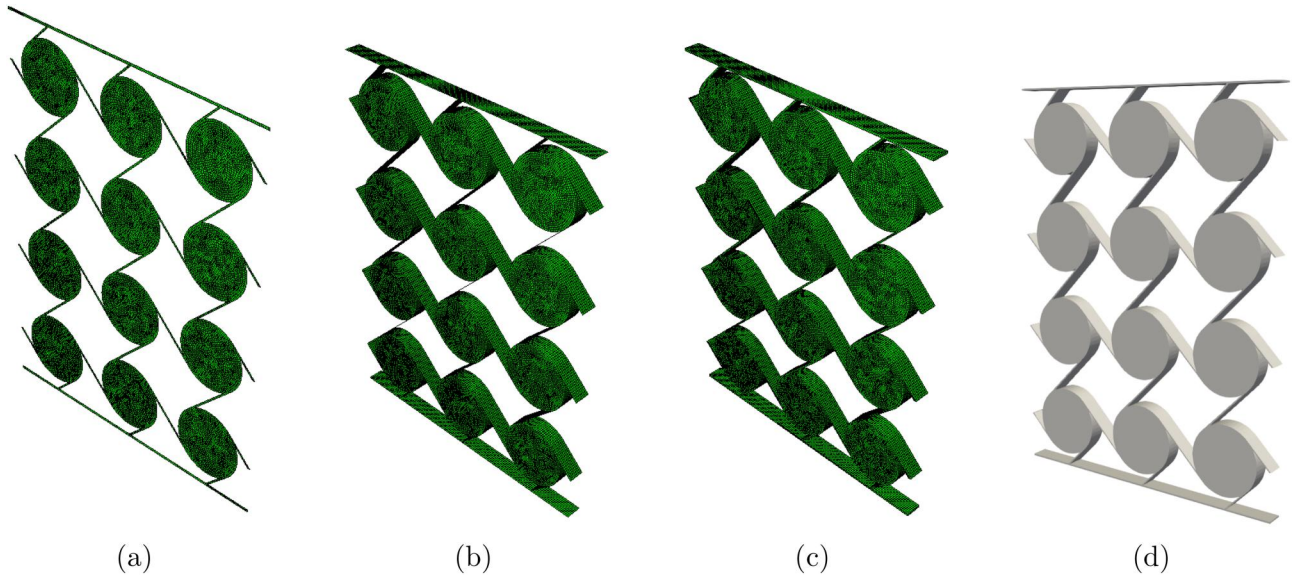


Figure 12. Numerical models of the second chiral metamaterial. 2D Abaqus models (a, b), 3D Abaqus model (c) and CUF 1D model (d).

approximately 38% of the DOFs required by the Abaqus 2D in–plane model (Figure 12a) and about 6% of those needed by the fully 3D Abaqus model (Figure 12c). The comparison of the deformed shapes in Figure 13 confirms that the CUF solution closely matches the high-fidelity 3D reference while retaining a significantly reduced computational cost, making it particularly suitable for extensive parametric studies on chiral architectures with varying infill and topology. This result, together with those obtained in the previous cases, demonstrate the reliability of CUF models, and so it will be used for the subsequent analyses.

5.2.2. Third chiral metamaterial

The last chiral metamaterial considered in this study is reported in Figure 14. In this configuration, the radius of the internal circles is set to $r_0 = 16$ mm. This example is

introduced to demonstrate that the proposed modeling framework can robustly handle highly intricate geometries, characterized by non-trivial connectivity and pronounced local rotations of the unit cells.

The structure is again clamped at the bottom plate and subjected to a compressive load applied at the top, in full analogy with the previous benchmarks. The corresponding deformed configuration is shown in Figure 15. The rotation of the intermediate circular cells, which is a key feature of the chiral response, is accurately captured by the model, together with the global bending and the local deformation of the ligaments. This final example thus confirms that the proposed approach remains effective and reliable even when dealing with chiral lattices of increasing geometric complexity, preserving its capability to reproduce both global and local kinematic mechanisms.

Table 3. DOFs and lateral displacement of the second chiral metamaterial. In blue the converged models.

Model	DOFs	Lateral displacement
Abaqus 2D (Figure 12a)	99,510	0.3904
	289,710	0.3843
	574,512	0.3844
Abaqus 2D + 3D (Figure 12b)	475,443	0.4050
	1,765,137	0.3490
	5,682,978	0.3487
Abaqus 3D (Figure 12c)	452,106	0.3429
	1,718,745	0.3886
	6,040,629	0.3896
CUF 1D (Figure 12d)	111,438	0.3816
	589,098	0.3818
	883,647	0.3820

5.3. Reentrant

The reentrant auxetic lattice considered in this section is shown in Figure 16, and its geometry is taken from [51]. The main geometric parameters of the unit cell are $L_1 = 10.5$ mm, $L_2 = 6.4$ mm, $t = 0.6$ mm, and an internal reentrant angle $\alpha = 60^\circ$.

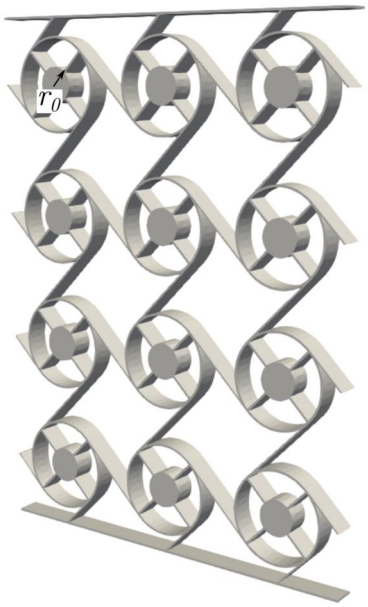


Figure 14. Geometry of the third chiral metamaterial metamaterial.

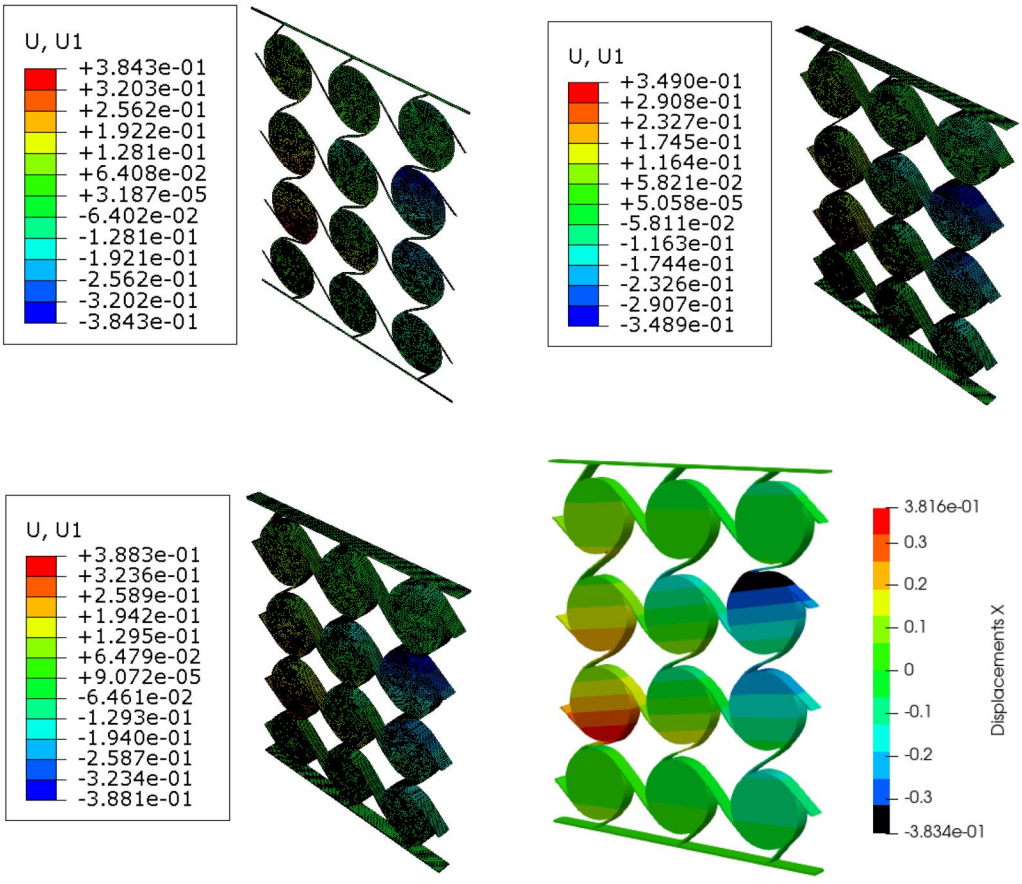


Figure 13. Numerical results of the second chiral metamaterial. 2D Abaqus models (top), 3D Abaqus model (bottom left) and CUF 1D model (bottom right).

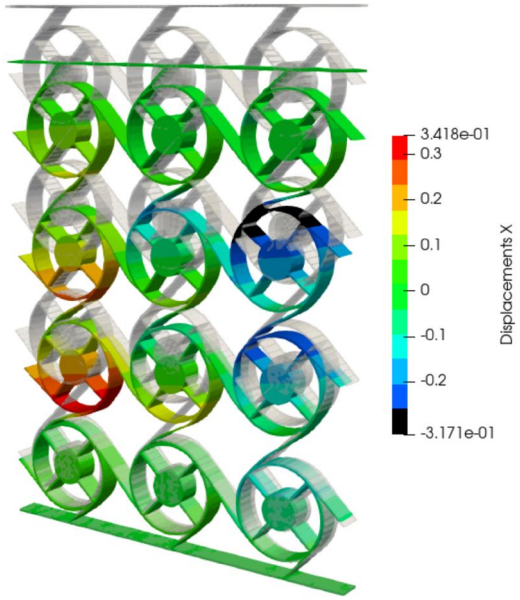


Figure 15. Numerical results of the third chiral metamaterial using CUF model.

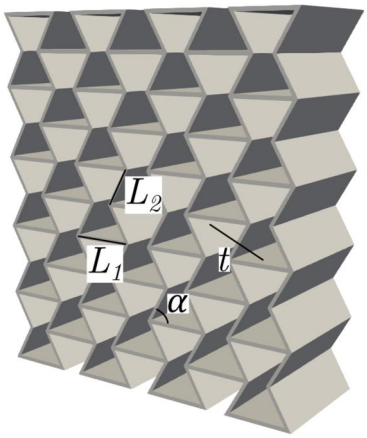


Figure 16. Geometry of the 2D reentrant metamaterial.

The structure is clamped at the bottom edge and subjected to a uniform compressive pressure applied on the top plate. The corresponding deformed configuration is reported in Figure 17. A pronounced lateral reduction is observed under vertical compression, which is the hallmark of a negative Poisson's ratio response and is typical of reentrant auxetic architectures. The numerical model captures very well the rotation and hinging of the inclined ligaments and the resulting transverse reduction, confirming its capability to reproduce the characteristic auxetic kinematics of this class of metamaterials.

5.4. 3D metamaterial

The last numerical example concerns a 3D extension of the 2D reentrant metamaterial. The case study is taken from [53], and the geometry of the unit cell is reported in Figure 18, together with a view of the full lattice. In that figure, the main geometric parameters are $L_1 = 6.2$ mm, $L_2 = 3.14$ mm, $t = 1$ mm, and a reentrant angle $\alpha = 70^{\circ}$.

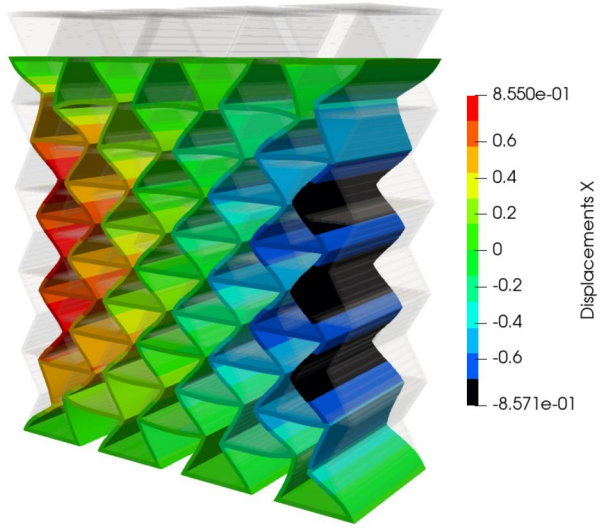


Figure 17. Numerical results of the 2D reentrant metamaterial using CUF model.

The structure is modeled entirely within the CUF framework. To construct such a complex three-dimensional geometry, a specific capability of CUF is exploited, namely the possibility of combining multiple one-dimensional beams within a single model. In this way, several distinct beam axes, each endowed with its own cross-sectional expansion and discretization, can be assembled to generate highly intricate architectures. In the present case, as illustrated in Figure 19, two beam axes are connected with alternating cross-sections. By enforcing the coincidence of the Lagrange interpolation points at the interface cross-sections, the kinematic compatibility between the beams is automatically guaranteed, without the need for additional constraint equations or coupling elements.

The lattice is subjected to a uniform compressive pressure applied at the top plate and clamped at the bottom, consistently with the previous benchmarks. The corresponding deformed configuration is depicted in Figure 20. The numerical results show a very low, almost vanishing, effective Poisson's ratio: under vertical compression, the transverse deformation remains small, indicating a quasi-zero Poisson response for this particular three-dimensional reentrant architecture. This example confirms that CUF can accurately capture the complex deformation mechanisms of auxetic metamaterials in three dimensions, while retaining full geometric flexibility. Moreover, the modeling strategy based on multiple interconnected beam axes suggests that CUF can be readily extended to simulate even more elaborate and large-scale metamaterial systems, including multilayered, graded, or hierarchical designs that would be extremely challenging to handle with conventional finite element formulations.

6. Conclusions

This work has assessed the capability of a CUF-based beam framework to model a broad class of mechanical metamaterials with hexagonal, chiral and reentrant architectures. A hierarchy of benchmark problems has been considered,

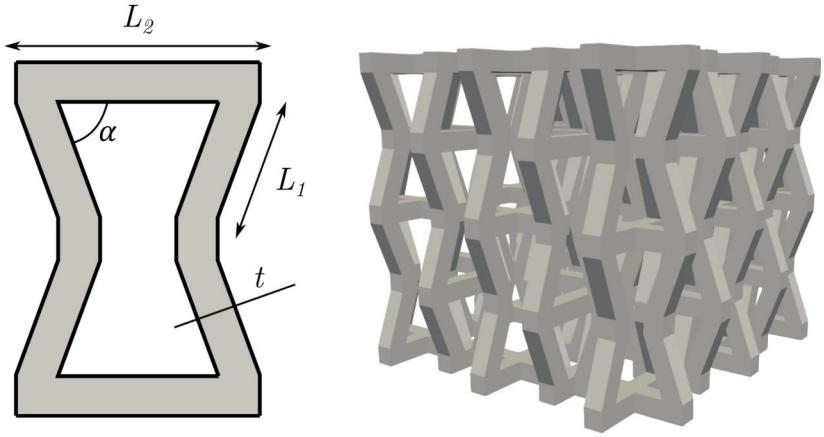


Figure 18. Geometry of the unit cell of the 3D reentrant metamaterial.

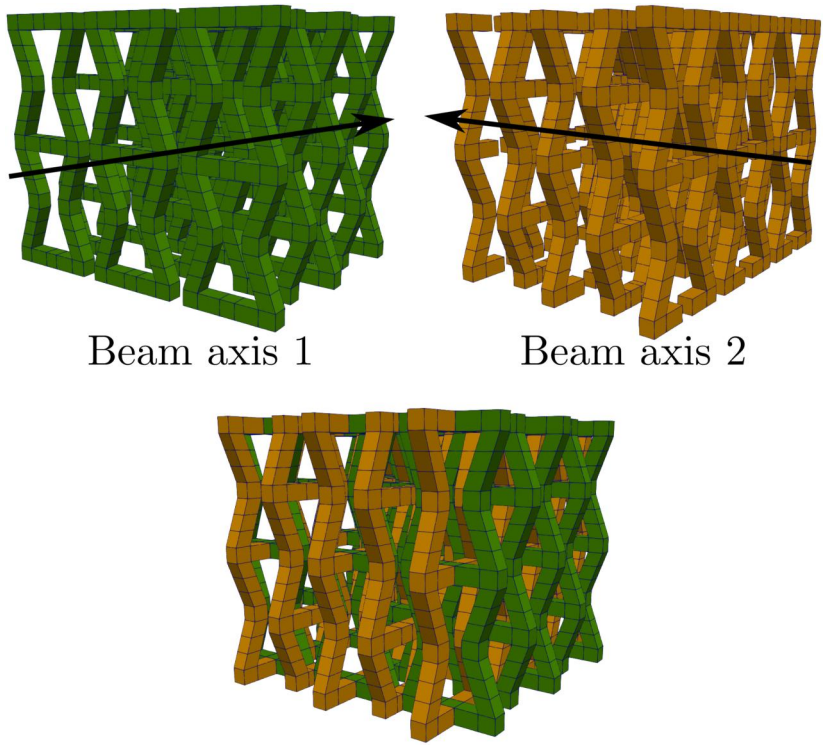


Figure 19. Modeling technique for the 3D reentrant metamaterial.

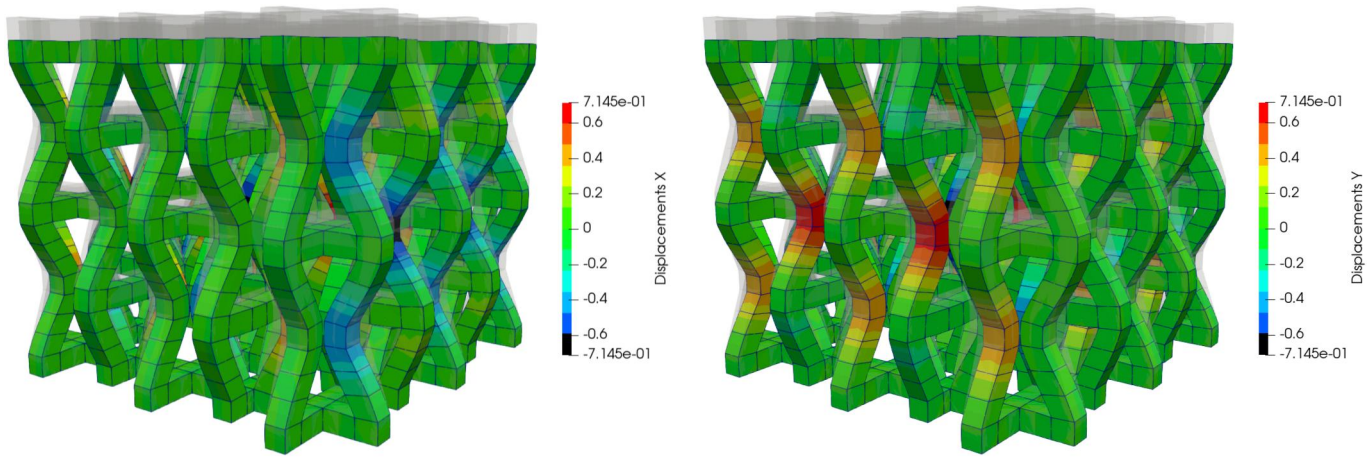


Figure 20. Numerical results of the 3D reentrant metamaterial.

ranging from two-dimensional chiral lattices with hollow unit cells to filled-cell variants and, finally, to a highly intricate chiral configuration featuring pronounced local rotations. These examples were complemented by classical two-dimensional reentrant auxetic honeycombs and by a fully three-dimensional reentrant lattice. In all cases, CUF results were systematically compared with those obtained from conventional 2D and 3D Abaqus models as for the hexagonal metamaterial. The results of this case are summarized in Figure 21, which summaries the values of the converged models

For the chiral lattices, it was shown that the proposed CUF formulation accurately reproduces the global response and the deformed configurations obtained from high-fidelity 3D finite element models. While a 2D Abaqus discretization along the width direction fails to provide reliable predictions even at very high numbers of degrees of freedom, the CUF models attain converged solutions with a substantially reduced computational cost. Depending on the configuration, reductions of the order of 50–80% in the number of DOFs were observed with respect to comparable 2D and 3D Abaqus models, with no loss of accuracy in the predicted displacements and deformation patterns, see Figure 22.

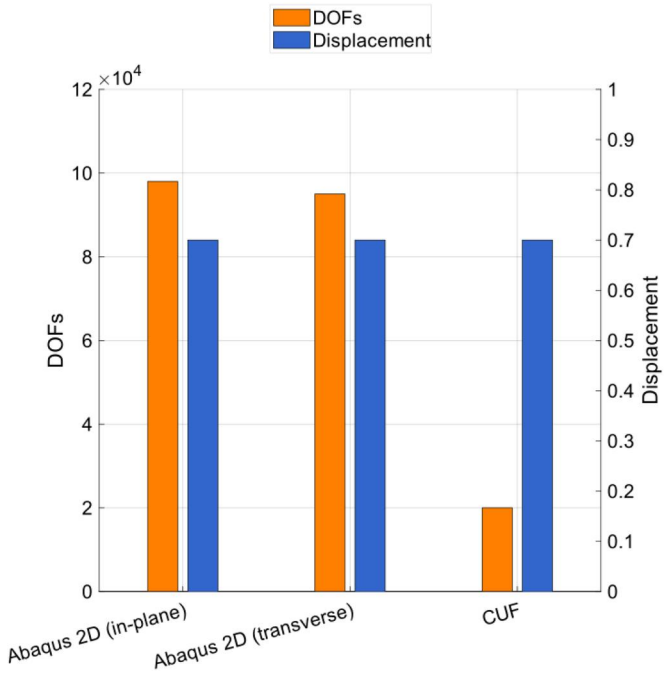


Figure 21. Summary of the results of the converged numerical models of the hexagonal metamaterial.

The most complex chiral example further demonstrated that the framework remains robust when handling geometries characterized by strong local rotations and non-trivial connectivity.

The reentrant auxetic benchmarks confirmed the ability of the CUF approach to capture distinctive metamaterial features at both the 2D and 3D levels. For the planar reentrant lattice, the model reproduced the expected lateral reduction under vertical compression, clearly exhibiting a negative Poisson's ratio that is typical of this class of structures. In the three-dimensional reentrant case, the combination of multiple beam axes with different cross-sectional expansions allowed the construction of a geometrically intricate lattice within a single CUF model. By enforcing the coincidence of Lagrange points at the interfaces, kinematic compatibility between beams was automatically guaranteed. The resulting simulations showed a very low, almost vanishing, effective Poisson's ratio, and demonstrated once again that complex auxetic mechanisms can be captured with a moderate number of DOFs.

Overall, the numerical evidence indicates that the CUF framework provides an effective and versatile tool for the analysis of chiral and reentrant metamaterials. It combines high accuracy with significant reductions in computational cost and offers a flexible modeling strategy, in which multiple interacting beams with tailored cross-sectional kinematics can be assembled to represent complex three-dimensional architectures. These features make CUF particularly attractive for large-scale parametric studies, design-oriented simulations, and the exploration of even more elaborate metamaterial concepts, including graded, hierarchical, and multi-functional lattice structures.

Author contributions

CRediT: **Riccardo Augello**: Conceptualization, Data curation, Formal analysis, Investigation, Methodology, Software, Validation, Writing –

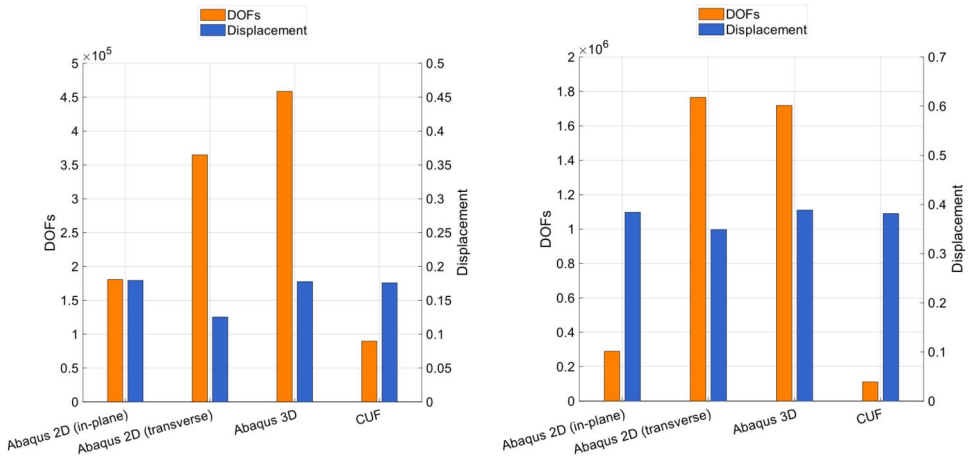


Figure 22. Summary of the results of the converged numerical models of the chiral metamaterials.

original draft, Writing – review & editing; **Erasmo Carrera**: Conceptualization, Data curation, Formal analysis, Investigation, Methodology, Project administration, Resources, Software, Supervision, Validation, Writing – original draft, Writing – review & editing.

Disclosure statement

No potential competing interest was reported by the author(s).

ORCID

Riccardo Augello http://orcid.org/0000-0002-3902-3272

References

[1] C. Zhao, Multi-plateau auxetic metamaterials with intra-and inter-cellular gradients for energy absorption, Aerotec Missili Spazio., vol. 105, no. 1, pp. 1–9, 2025.

[2] K. Bertoldi, P.M. Reis, S. Willshaw, and T. Mullin, Negative Poisson's ratio behavior induced by an elastic instability, Adv. Mater., vol. 22, no. 3, pp. 361–366, 2010. DOI: 10.1002/adma.200901956.

[3] T.A.M. Hewage, K.L. Alderson, A. Alderson, and F. Scarpa, Double-negative mechanical metamaterials displaying simultaneous negative stiffness and negative Poisson's ratio properties, Adv. Mater., vol. 28, no. 46, pp. 10323–10332, 2016. DOI: 10.1002/adma.201603959.

[4] L. Ai, and X.-L. Gao, Metamaterials with negative Poisson's ratio and non-positive thermal expansion, Compos. Struct., vol. 162, pp. 70–84, 2017. DOI: 10.1016/j.compstruct.2016.11.056.

[5] M. Kadic, T. Bückmann, N. Stenger, M. Thiel, and M. Wegener, On the practicability of pentamode mechanical metamaterials, Appl. Phys. Lett., vol. 100, no. 19, pp. 191901, 2012. DOI: 10.1063/1.4709436.

[6] B. Florijn, C. Coulais, and M. van Hecke, Programmable mechanical metamaterials, Phys. Rev. Lett., vol. 113, no. 17, pp. 175503, 2014. DOI: 10.1103/PhysRevLett.113.175503.

[7] A. Rafsanjani, A. Akbarzadeh, and D. Pasini, Snapping mechanical metamaterials under tension, Ad. Mater., vol. 27, no. 39, pp. 5931–5935, 2015. doi: 10.1002/adma.201502809.

[8] A. Rafsanjani, and D. Pasini, Bistable auxetic mechanical metamaterials inspired by ancient geometric motifs, Extreme Mech. Lett., vol. 9, pp. 291–296, 2016. DOI: 10.1016/j.eml.2016.09.001.

[9] B. Haghpanah, L. Salari-Sharif, P. Pourrajab, J. Hopkins, and L. Valdevit, Multistable shape-reconfigurable architected materials, Adv. Mater., vol. 28, no. 36, pp. 7915–7920, 2016. DOI: 10.1002/adma.201601650.

[10] E. Rustighi, P. Gardonio, S. Baldini, C. Malacarne, and M. Perini, Material characterisation of deflated structured fabrics, Aerotec. Missili Spaz., vol. 104, no. 3, pp. 247–256, 2025. DOI: 10.1007/s42496-024-00228-2.

[11] K. Che, C. Yuan, J. Wu, H. Jerry Qi, and J. Meaud, Three-dimensional-printed multistable mechanical metamaterials with a deterministic deformation sequence, J. Appl. Mech., vol. 84, no. 1, pp. 011004, 2017. DOI: 10.1115/1.4034706.

[12] M. Bodaghi, A.R. Damanpack, and W.H. Liao, Self-expanding/shrinking structures by 4D printing, Smart Mater. Struct., vol. 25, no. 10, pp. 105034, 2016. DOI: 10.1088/0964-1726/25/10/105034.

[13] E. Ptochos, and G. Labeas, Elastic modulus and Poisson's ratio determination of micro-lattice cellular structures by analytical, numerical and homogenisation methods, J. Sandwich Struct. Mater., vol. 14, no. 5, pp. 597–626, 2012. DOI: 10.1177/1099636212444285.

[14] S.M. Ahmadi, G. Campoli, S. Amin Yavari, B. Sajadi, R. Wauthle, J. Schrooten, H. Weinans, and A.A. Zadpoor, Mechanical behavior of regular open-cell porous biomaterials made of diamond lattice unit cells, J. Mech. Behav. Biomed. Mater., vol. 34, pp. 106–115, 2014. DOI: 10.1016/j.jmbbm.2014.02.003.

[15] R. Hedayati, M. Sadighi, M. Mohammadi-Aghdam, and A.A. Zadpoor, Mechanical properties of regular porous biomaterials made from truncated cube repeating unit cells: analytical solutions and computational models, Mater. Sci. Eng. C Mater. Biol. Appl., vol. 60, pp. 163–183, 2016. DOI: 10.1016/j.msec.2015.11.001.

[16] H. Wan, H. Ohtaki, S. Kotosaka, and G. Hu, A study of negative Poisson's ratios in auxetic honeycombs based on a large deflection model, Eur. J. Mech.-A/Solids, vol. 23, no. 1, pp. 95–106, 2004. DOI: 10.1016/j.euromechsol.2003.10.006.

[17] C. Körner, and Y. Liebold-Ribeiro, A systematic approach to identify cellular auxetic materials, Smart Mater. Struct., vol. 24, no. 2, pp. 025013, 2015. DOI: 10.1088/0964-1726/24/2/025013.

[18] F. Warmuth, F. Osmanlic, L. Adler, M.A. Lodes, and C. Körner, Fabrication and characterisation of a fully auxetic 3D lattice structure via selective electron beam melting, Smart Mater. Struct., vol. 26, no. 2, pp. 025013, 2017. DOI: 10.1088/1361-665X/26/2/025013.

[19] D. Li, J. Yin, L. Dong, and R.S. Lakes, Numerical analysis on mechanical behaviors of hierarchical cellular structures with negative Poisson's ratio, Smart Mater. Struct., vol. 26, no. 2, pp. 025014, 2017. DOI: 10.1088/1361-665X/26/2/025014.

[20] J. Hou, D. Li, and L. Dong, Mechanical behaviors of hierarchical cellular structures with negative Poisson's ratio, J. Mater. Sci., vol. 53, no. 14, pp. 10209–10216, 2018. DOI: 10.1007/s10853-018-2298-0.

[21] J. Schwerdtfeger, P. Heinl, R.F. Singer, and C. Körner, Auxetic cellular structures through selective electron-beam melting, Phys. Status Solidi (b), vol. 247, no. 2, pp. 269–272, 2010. DOI: 10.1002/pssb.200945513.

[22] J. Schwerdtfeger, F. Wein, G. Leugering, R.F. Singer, C. Körner, M. Stingl, and F. Schury, Design of auxetic structures via mathematical optimization, Adv. Mater., vol. 23, no. 22–23, pp. 2650–2654, 2011. DOI: 10.1002/adma.201004090.

[23] T. Bückmann, N. Stenger, M. Kadic, J. Kaschke, A. Frölich, T. Kennerknecht, C. Eberl, M. Thiel, and M. Wegener, Tailored 3D mechanical metamaterials made by dip-in direct-laser-writing optical lithography, Adv. Mater., vol. 24, no. 20, pp. 2710–2714, 2012. DOI: 10.1002/adma.201200584.

[24] L. Yang, O. Harrysson, H. West, and D. Cormier, Compressive properties of ti–6al–4v auxetic mesh structures made by electron beam melting, Acta Mater., vol. 60, no. 8, pp. 3370–3379, 2012. DOI: 10.1016/j.actamat.2012.03.015.

[25] X. Li, Z. Lu, Z. Yang, and C. Yang, Directions dependence of the elastic properties of a 3D augmented re-entrant cellular structure, Mater. Des., vol. 134, pp. 151–162, 2017. DOI: 10.1016/j.matdes.2017.08.024.

[26] X.-T. Wang, X.-W. Li, and L. Ma, Interlocking assembled 3D auxetic cellular structures, Mater. Des., vol. 99, pp. 467–476, 2016. DOI: 10.1016/j.matdes.2016.03.088.

[27] K.W. Wojciechowski, Two-dimensional isotropic system with a negative Poisson ratio, Phys. Lett. A., vol. 137, no. 1–2, pp. 60–64, 1989. DOI: 10.1016/0375-9601(89)90971-7.

[28] D. Prall, and R.S. Lakes, Properties of a chiral honeycomb with a Poisson's ratio of—1, Int. J. Mech. Sci., vol. 39, no. 3, pp. 305–314, 1997. DOI: 10.1016/S0020-7403(96)00025-2.

[29] A. Alderson, K.L. Alderson, D. Attard, K.E. Evans, R. Gatt, J.N. Grima, W. Miller, N. Ravirala, C.W. Smith, and K. Zied, Elastic constants of 3-, 4-and 6-connected chiral and anti-chiral honeycombs subject to uniaxial in-plane loading, Compos. Sci. Technol., vol. 70, no. 7, pp. 1042–1048, 2010. DOI: 10.1016/j.compscitech.2009.07.009.

[30] A. Spadoni, M. Ruzzene, and F. Scarpa, Dynamic response of chiral truss-core assemblies, J. Intell. Mater. Syst. Struct., vol. 17, no. 11, pp. 941–952, 2006. DOI: 10.1177/1045389X06060219.

[31] K.F. Tee, A. Spadoni, F. Scarpa, and M. Ruzzene, Wave propagation in auxetic tetrachiral honeycombs, J. Vib. Acoust., vol. 132, no. 3, pp. 031007, 2010. DOI: 10.1115/1.4000785.

[32] T. Frenzel, J. Köpfler, E. Jung, M. Kadic, and M. Wegener, Ultrasound experiments on acoustical activity in chiral mechanical metamaterials, Nat. Commun., vol. 10, no. 1, pp. 3384, 2019. DOI: 10.1038/s41467-019-11366-8.

[33] K. Zhang, P. Zhao, C. Zhao, F. Hong, and Z. Deng, Study on the mechanism of band gap and directional wave propagation of the auxetic chiral lattices, Compos. Struct., vol. 238, pp. 111952, 2020. DOI: 10.1016/j.compstruct.2020.111952.

[34] A. Spadoni, M. Ruzzene, S. Gonella, and F. Scarpa, Phononic properties of hexagonal chiral lattices, Wave Motion., vol. 46, no. 7, pp. 435–450, 2009. DOI: 10.1016/j.wavemoti.2009.04.002.

[35] A. Spadoni, and M. Ruzzene, Structural and acoustic behavior of chiral truss-core beams, World Acad. Sci. Eng. Technol., vol. 128, no. 5, pp. 616–626, 2006. DOI: 10.1115/1.2202161.

[36] F. Maurin, F. Greco, and W. Desmet, Isogeometric analysis for nonlinear planar pantographic lattice: discrete and continuum models, Continuum Mech. Thermodyn., vol. 31, no. 4, pp. 1051–1064, 2019. DOI: 10.1007/s00161-018-0641-y.

[37] Y. Wang, H. Xu, and D. Pasini, Multiscale isogeometric topology optimization for lattice materials, Comput. Methods Appl. Mech. Eng., vol. 316, pp. 568–585, 2017. DOI: 10.1016/j.cma.2016.08.015.

[38] Y. Wang, Z. Wang, Z. Xia, and L.H. Poh, Structural design optimization using isogeometric analysis: a comprehensive review, Comput. Model. Eng. Sci., vol. 117, no. 3, pp. 455–507, 2018. DOI: 10.31614/cmes.2018.04603.

[39] F. Vlădulescu, and D.M. Constantinescu, Lattice structure optimization and homogenization through finite element analyses, Proc. Inst. Mech. Eng., L, vol. 234, no. 12, pp. 1490–1502, 2020. DOI: 10.1177/1464420720945744.

[40] J. Somnic, and B.W. Jo, Status and challenges in homogenization methods for lattice materials, Materials, vol. 15, no. 2, pp. 605, 2022. DOI: 10.3390/ma15020605.

[41] S. Arabnejad, and D. Pasini, Mechanical properties of lattice materials via asymptotic homogenization and comparison with alternative homogenization methods, Int. J. Mech. Sci., vol. 77, pp. 249–262, 2013. DOI: 10.1016/j.ijmecsci.2013.10.003.

[42] S. Lin, J. Cai, H. Xia, X. Ao, and J. Liu, A reduced-order model based on finite element method for fast prediction of thermal performance of lattice structures, Int. Commun. Heat Mass Transfer., vol. 126, pp. 105347, 2021. DOI: 10.1016/j.icheatmasstransfer.2021.105347.

[43] S. McBane, and Y. Choi, Component-wise reduced order model lattice-type structure design, Comput. Methods Appl. Mech. Eng., vol. 381, pp. 113813, 2021. DOI: 10.1016/j.cma.2021.113813.

[44] E. Carrera, G. Giunta, and M. Petrolo, Beam Structures: Classical and Advanced Theories, John Wiley & Sons, New York, NJ, 2011.

[45] E. Carrera, M. Cinefra, M. Petrolo, and E. Zappino, Finite Element Analysis of Structures through Unified Formulation, John Wiley & Sons, Chichester, West Sussex, UK, 2014.

[46] R. Augello, and E. Carrera, Nonlinear dynamics and band gap evolution of thin-walled metamaterial-like structures, J. Sound Vib., vol. 578, pp. 118329, 2024. DOI: 10.1016/j.jsv.2024.118329.

[47] R. Augello, E. Carrera, W.Q. Chen, B. Wu, and Y.Z. Wang, Nonlinear static analysis of metamaterial structures based on the kagome lattice using beam finite elements and component-wise approach, Int. J. Solids Struct., vol. 318, pp. 113387, 2025. DOI: 10.1016/j.ijsolstr.2025.113387.

[48] J.N. Reddy, Mechanics of Laminated Composite Plates and Shells. Theory and Analysis, 2nd ed., CRC Press, Boca Raton, FL, 2004.

[49] K.J. Bathe, Finite Element Procedure, Prentice Hall, Upper Saddle River, NJ, 1996.

[50] E. Carrera, M. M. Cinefra, M. Petrolo, and E. Zappino, Finite Element Analysis of Structures through Unified Formulation, John Wiley Sons, Hoboken, NJ, 2014.

[51] W. Hou, P. He, Y. Yang, and L. Sang, Crashworthiness optimization of crash box with 3D-printed lattice structures, Int. J. Mech. Sci., vol. 247, pp. 108198, 2023. DOI: 10.1016/j.ijmecsci.2023.108198.

[52] H. Ruan, J. Hou, and D. Li, Wave propagation characterization of 2D composite chiral lattice structures with circular plate inclusions, Eng. Struct., vol. 264, pp. 114466, 2022. DOI: 10.1016/j.engstruct.2022.114466.

[53] J. Shen, K. Liu, Q. Zeng, J. Ge, Z. Dong, and J. Liang, Design and mechanical property studies of 3D re-entrant lattice auxetic structure, Aerosp. Sci. Technol., vol. 118, pp. 106998, 2021. DOI: 10.1016/j.ast.2021.106998.